Available online at www.ijournalse.org

Emerging Science Journal

(ISSN: 2610-9182)

Vol. 7, No. 4, August, 2023

Mapping of Sensing Performance of Concentric and Non-Concentric Silver Nanoring

Mulda Muldarisnur [1*], Ilham Perdana [1], E. Elvaswer [1], Dwi Puryanti [1]

[1] *Department of Physics, Faculty of Mathematics and Natural Sciences, Universitas Andalas, Padang 25163, Indonesia.*

Abstract

Sensors play a critical role in improving overall human quality of life. They have been employed in most aspects of our lives. A recently emerging sensing platform is based on plasmonic resonance at the boundary of metals and dielectrics. Localized surface plasmon resonances–based sensors offer miniaturization, a simple setup, and relatively high sensitivity for real-time measurements. The reported figure of merit (FOM) of the LSPR-based sensor is generally limited, primarily due to its broad resonance peak. Nanorings composed of metal nanoparticles are known for their broad-range resonance tunability, high field localization, and large sensing area. Asymmetry of the nanoring with the introduction of core offset relaxes the selection rule for mode mixing, thus resulting in a narrower resonance peak. This may overcome broad resonance peak restriction. Concentric and non-concentric nanorings were simulated using the boundary element method implemented with the MNPBEM toolbox. We map the performance of nanoring sensors over a wide range of geometrical variations, namely, diameter, ring shell thickness, and the offset of the inner ring to the center of the outer ring wall (core offset). Sensitivity and FOM were found to rely substantially on the nanoring size parameters. The sensing performance map helps to obtain optimized nanoring parameters for the intended spectral range region. The obtained high sensitivity and FOM are much higher than the data available in the literature over visible and NIR ranges. The findings demonstrate the potential of nanorings for biosensing applications.

Keywords:

Localized Surface Plasmon Resonance;
Nanoring;
Sensing;
Sensitivity; Biosensors;
The Figure of Merit.

Article History:

Received:	06	February	2023
Revised:	26	April	2023
Accepted:	09	June	2023
Available online:	12	July	2023

1- Introduction

Modern society benefits a lot from advances in sensing technology. Developed sensing technologies have been proven to ease and enhance the quality of human life. They have been used to develop smart cities, smart homes, industry, health monitoring, and many others. A sensor detects environmental changes and then uses this information as electrical or optical signals to obtain a measured quantity. Sensors have vast applications, including, but not limited to, biochemical sensing [1, 2], the pharmaceutical industry [3], security and defense [4], medical diagnosis [5, 6], manufacturing [7], automotive [8], research [9, 10], the food industry [11], and environmental monitoring [12]. The past two years have seen great progress in detecting viruses and hazardous materials in response to the COVID-19 outbreak. Developing efficient and effective drugs or vaccines requires a clear understanding of the specific interactions and binding kinetics between biochemical molecules, proteins, and cells. These examples show the importance of high-performance biosensors that can accurately detect ultra-small quantities of molecules label-free and in real-time to anticipate possible health threats in the future [13].

The signal detected shows that biosensors are classified into four distinct categories, namely, electrochemical, piezoelectric, magnetic, and optical sensors [14]. Compared to others, optical biosensors are the most widely used for analytical biosensing in the laboratory due to their great sensitivity, high specificity, multiplexing possibility, and low

* **CONTACT**: muldarisnur@sci.unand.ac.id

DOI: http://dx.doi.org/10.28991/ESJ-2023-07-04-04

noise with a small amount of sample [15, 16]. Optical-type biosensors have several forms: fluorescent, electro-luminescent, photoluminescent, colorimetric, and plasmonic [17]. Fluorescent spectroscopy is exceptionally sensitive and selective. The fluorescent techniques' disadvantages are the need to label species, the relatively time-consuming, and the applicability only to small molecules. Electro and photoluminescent spectroscopies exhibit moderate sensitivity and selectivity over a wide detection range but are cost-intensive, slow, and require complicated sample preparation. The colorimetric technique, which is fast and inexpensive, suffers from low reproducibility and selectivity. These limitations can be avoided by plasmonic-based sensing.

Surface plasmons can be thought of as oscillations of conduction electrons in a metallic nanostructure when excited with light having an appropriate wavelength. The oscillations result in strong absorption and light scattering, local electric field enhancement, and nanometer-scale light confinement around metal surfaces [18]. Plasmonic excitation enables sub-wavelength light focusing that may overcome the optical diffraction limit to realize highly sensitive plasmonic-based sensors at a miniaturized size [18–20]. Unique optical properties enable metallic nanostructures to be applied in several applications, including chemical and biological sensing [21, 22], field-enhanced spectroscopies [23, 24], solar energy harvesting [25, 26], medical diagnostics [27], photothermal therapy [28], drug screening and testing [29], and integrated optical devices [30].

Plasmonic-based sensing has gained popularity recently due to its extremely high sensitivity [31], simple and inexpensive instruments [32], high compatibility with analytes, broad working spectral range, less sensitivity to bulk noises [33], real-time, label-free [18, 34–36], and the possibility of high-density multiplexing using microfluidic chips [33, 37, 38]. Using the right nanoparticle material, size, shape, and arrangement, it is feasible to achieve high lateral resolution and a broad spectral range. Small molecules can be detected because of the shallow penetrability of plasmon oscillations into the surrounding medium. It is essential to be able to detect tiny molecules in order to construct compact, spatially targeted sensors that are highly sought-after for biological applications. In general, labeling is performed by attaching tagging species (e.g., biotin, enzymes, dyes, or fluorophores) to the target biomolecules, which may influence the affinities of the labeled molecules and, subsequently, the measurement findings. In contrast, label-free detection enables sensitive assessment of target analytes in real-time and on-site without complex sample handling and equipment [18, 39, 40]. For plasmonic-based sensors, label-free detection is achievable because the electric field around the nanoparticle is significantly enhanced, allowing signal amplification from the target molecule. In addition, unlike typical fluorophores, metallic nanoparticles do not blink or bleach, allowing for long-term monitoring.

Plasmonic sensors rely mostly on the change in the resonance peak. The shift might be caused by the direct adsorption of molecules or by the selective binding of analyte molecules to the chemically functionalized nanoparticle surface. The optical response of metallic nanoparticles is often dominated by dipolar modes highly dependent on the particle's shape, size, and index of refraction at medium wavelengths. In addition to the sphere [41], pyramid [41], ellipsoid [42], donut [43], cube [44], rod [45, 46], bar [47], rice [47], triangle [48], triangular prisms [49], branched nanoparticles [50], stars [51, 52], rings [53, 54], and disc [55], noble metal nanoparticles have been synthesized or manufactured in numerous geometrical shapes. The detection capability of localized surface plasmon resonance sensors is constrained by a wide resonance peak width caused by radiative dampening [35]. Broad resonance peaks prevent precise measurements, particularly at low analyte concentrations. In addition, the damping reduces the strength of localized electromagnetic fields surrounding nanoparticles.

Using an array of nanoparticles [32, 35], concentric nanocavities [55, 56], closely packed nanoparticle clusters [57, 58], metamaterials [59], and asymmetric nanoparticles [56, 60] are some of the suggested solutions to the wide resonance problem. Instead of decaying into free space, the narrow peak in an array and cluster of nanoparticles results from the recovered scattered field of one particle by its neighbor. The downside of metal nanoclusters and metamaterials is that their manufacturing requires lithographic procedures. Due to the simplicity of wet chemical production, single solid or shell nanoparticles are frequently used. Due to interference between narrow dark and wide brilliant modes [61], asymmetric or linked nanoparticles display a narrow Fano resonance. The short line width and significant improvement of the near-field improve the sensing performance. Local field enhancement and resonance spectra of metal nanoparticles have been computed utilizing a variety of techniques, including the finite element approach, finite difference time domain, discrete dipole approximation, boundary element method, and multi-layered Mie theory [62–64]. The sensing sensitivity and figure of merit (FOM) of solid and symmetric spherical shell structures have been the subject of several studies. To date, however, no theoretical work has been published that maps the sensing performance of asymmetric core-shell architectures. Finding the optimal particle shape and size, resulting in high sensitivity and FOM, is crucial for low-cost and real-time sensing [65, 66].

In this study, the sensitivity and FOM of silver nanorings are optimized. As a result of the hybridization of plasmon modes supported by the inner and outer surfaces of the nanoshell, the nanoring provides a greater degree of tuning of the resonance wavelength. The plasmon resonance of a nanoring is dependent on the dielectric constant of the core and shell material, the diameter of the core, the thickness of the metal shell, and the index of refraction of the surrounding medium [21, 23]. The resonance wavelength of nanorings may be set to the near-infrared water window, where tissue

and blood are transparent, allowing for an array of nano-biomedical advancements. The introduction of asymmetry by offsetting the core of a nanoring relaxes the selection rule for mode mixing [56, 67–69], permitting a bigger shift of the resonance wavelength with a medium refractive index and the activation of a narrow peak Fano resonance. Asymmetric nanoparticles have a greater sensitivity to the refractive index and smaller resonance peaks. We discovered that the diameter, shell thickness, and core offset strongly impact local field enhancement, sensing sensitivity, and the FOM of nanoring biosensors, allowing for exceptionally high sensing performance. Particularly for diagnostics, bioanalytical sensing devices should have high sensitivity. In contrast, a high FOM correlates to a lower detectable concentration limit for analytes. The sensitivity and FOM of non-concentric nanorings produced in this study are greater than those reported in prior studies for localized surface plasmon resonance-based sensors.

2- Methods

2-1- Simulation Details

The simulated structures of silver nanorings are presented in Figure 1. The ring comprises an air core of radius (R_i) and a silver shell with a radius of (R_o). The outer diameter of the nanoring varied from 10–60 nm, with a step of 10 nm. The nanoring shell thickness was fine-tuned by changing the inner shell radius normalized to the outer radius (R_i / R_o =.3, .5, .7, and .9). In addition to the concentric structure, the core offset (δ) along the x-axis was introduced to induce asymmetry. The maximum core offset δ_{max} equals the shell thickness (R_o - R_i) when a nanoring turns into a nano-crescent. In the simulation, the core offset was normalized to its maximum value for each nanoring diameter: 0, 0.2, 0.4, 0.6, 0.8, and 1.0. The nanoring height was constant at 5 nm. The dielectric constant of silver was adopted from the work of Johnson & Christy [70], while the dielectric constant of the surrounding medium was assumed to be wavelength-independent, with values ranging from 1.0 to 2.0.

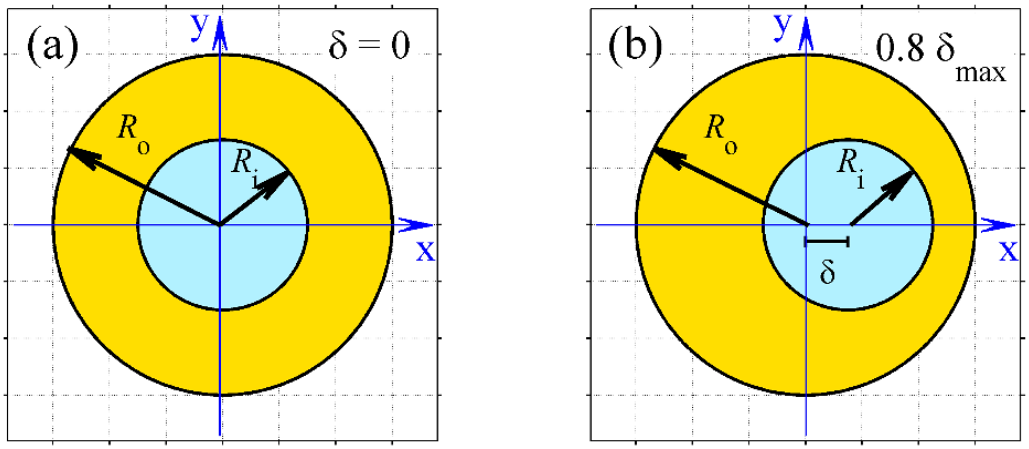

Figure 1. Simulated structures, (a) concentric, and (b) non-concentric silver nanoring

Using the boundary element approach [71, 72] integrated in the MNPBEM toolbox [73, 74], the simulation was conducted. To acquire the extinction cross-section spectra of the nanoring, the retarded solver was selected to solve the full solution of Maxwell's equations. Using an electric field, a plane wave incident along the z-axis was polarized along the y-axis. With this configuration, nanoring height has no effect on resonance qualities. The extinction spectra for nanorings with a diameter of less than 30 nm were determined between 300 and 1500 nm. For bigger nanorings, calculations up to 3500 nm were undertaken. The simulated wavelength resolution was 1 nm. Polarization and the direction of entering plane waves were held constant throughout all computations.

2-2- Determination of Sensing Performances

The sensitivity to the refractive index and the figure of merit (FOM) characterise the efficiency of plasmonic-based sensors [75, 76]. The sensitivity is the shift (or gradient) of the plasmon resonance peak wavelength (λ_{res}) induced by the change inside the local refractive index (n) of the medium. The unit of sensitivity is nm/RIU, where RIU is the unit of refractive index.

$$S = \frac{d\lambda_{res}}{dn} \quad (1)$$

The Refractive index of the medium was in the range of 1.0 – 2.0. The sensitivity for every refractive index was computed from the resonance peak shift as a function of the refractive index with the central difference approximation, with the exception of those at refractive index values of 1 and 2, which were estimated by the forward and backward difference, respectively.

A larger nanoparticle shows a stronger redshift and extinction of the resonance peak, thus creating a greater sensitivity and a wider peak, which in turn results in a reduced spectral contrast. A narrower spectral peak is needed for sensing applications, since it has a greater accuracy. Another parameter, the FOM, is set as the sensitivity to peak width ratio (or full width at half maximum (or FWHM)), known as:

$$FOM = \frac{dS}{FWHM} \tag{2}$$

High FOM readings are indicative of a well-performing sensor. FOM is inversely related to the detection limit, which is the smallest change in refractive index that can be observed [77]. FOM is more commonly used to compare the performance of various sensor types than sensitivity. Continuous attempts have been made to increase and maximise sensitivity and FOM in order to achieve an ultralow detection limit.

Figure 2 depicts the simulation procedure's flowchart. For each nanoring diameter, we changed shell thickness (specified by inner ring radius) and core offset. To calculate sensitivity, the medium's index of refraction was altered for every combination of nanoring geometrical parameters. Spectra of extinction were computed using the MNPBEM toolkit [73].

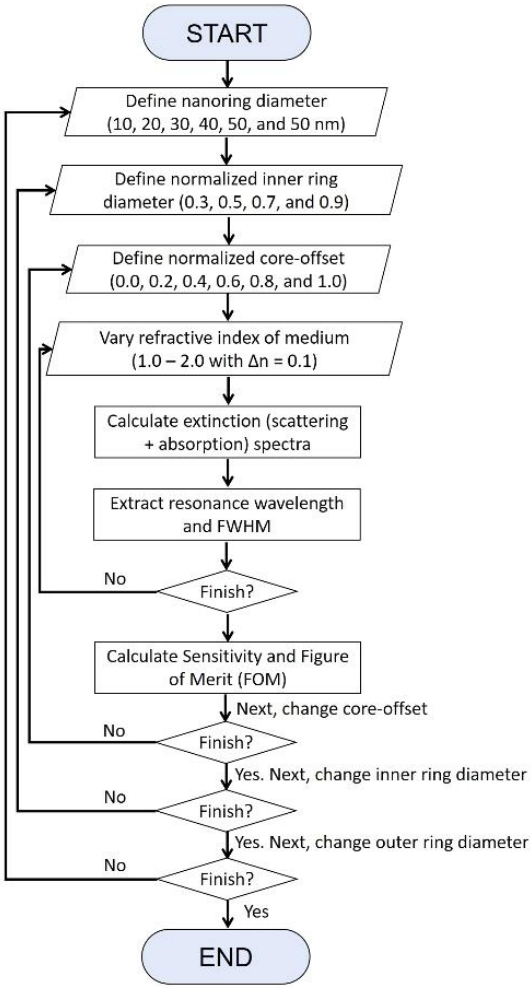

Figure 2. Flow chart of the simulation process

3- Results and Discussion

3-1- Extinction Peak, Resonance Wavelength, and Peak Width

The zoom resonance spectra of nanorings with an outer diameter of 20 nm for different inner ring radiuses and core offsets are presented in Figure 3. The spectra for other nanoring diameters are given in supporting information. The resonance peak is red-shifted with nanoring diameter, shell thickness (inner ring radius), and core offset. Increasing the inner ring radius (or equivalent to a reduced shell thickness) causes more redshift compared to the core offset for a fixed nanoring diameter. Higher-order peaks at shorter wavelengths are more prominent for larger core offsets. The maximum extinction tends to increase with nanoring diameter. The dependence of the maximum extinction on core offset is not linear; it tends to increase and then decrease. The complete map of extinction maximum as a function of nanoring diameter and core offset is given in Supporting information.

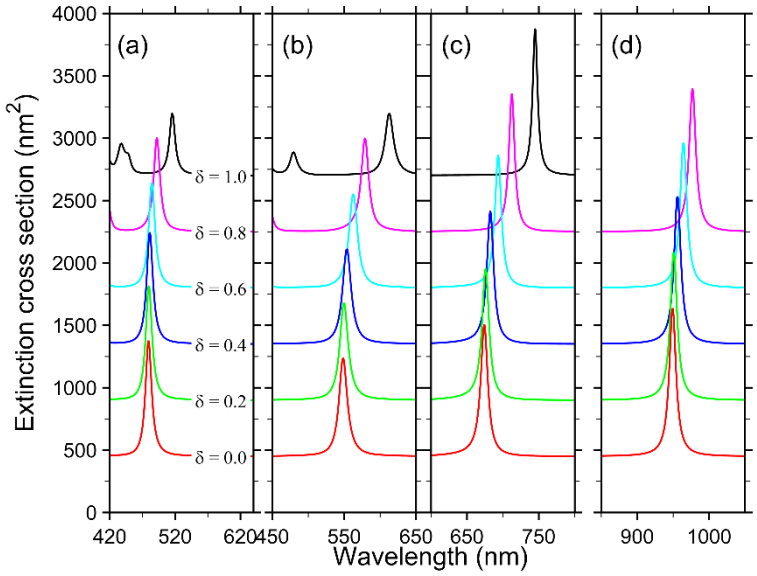

Figure 3. Extinction spectra of silver nanoring of outer diameter 10 nm for different normalized inner ring radius Ri, (a) 0.3 R_o, (b) 0.5 R_o, (c) 0.7 R_o, and (d) 0.9 R_o. The refractive index was set as 1.4. The offset of the inner ring δ for all subplots is the same as in figure (a). Spectra are shifted upward for better comparison.

The oscillating electric field of light causes the free electrons of metal nanoparticles to oscillate when they are illuminated. The oscillation of electrons around a particle's surface separates it from its positively charged metallic core, generating a dipole oscillation along the polarization of the electric field. The positive metal core produces a restoring force proportionate to the distance between the electrons. Maximum electron oscillation amplitude occurs at a certain wavelength, known as the resonance wavelength. The resonance wavelength is dependent on the material qualities, size, and shape of the medium surrounding the nanoparticle, as well as its refractive index. In the case of connected or arrayed nanoparticles, the spacing and arrangement of nanoparticles, as well as the direction of light polarization, also affect the resonance wavelength. The redshift of the resonance peak as a function of particle diameter can be explained by a reduction in the restoring force on oscillating electrons. With increasing distance from the center of mass of electrons and positive ions in metal, the restoring force diminishes. The redshift associated with the core offset is the result of a higher interaction between the inner and outer shell resonant modes. Two factors contribute to the overall energy loss (extinction) of illuminating light: material absorption and scattering. Cross sections of extinction (i.e., scattering and absorption) depend on particle size [78]. Small nanoparticles (i.e., less than 25 nm) have a tendency to waste photon energy via inelastic processes; hence, absorption predominates. Contrarily, scattering is more dominant for nanoparticles that are larger in size. The energy of photons will be employed to induce electron oscillation, followed by the emission of light with the same wavelength.

Multipoles of plasmon modes engage with modes with the same order in concentric nanorings (=0); dipolar disc modes hybridize exclusively with dipolar cavity modes [79]. This constraint is eased for non-concentric nanorings that permit mode interactions with varying order. This mixing makes the higher-order plasmon modes of nanorings with a bigger core offset more apparent. Plasmon hybridization theory disassembles a composite nanostructure into two or more elementary geometries before calculating the composite's resonance frequency based on the interactions between the elementary geometries. This theory is accurate and intuitive, analogous to the bonding of atoms in a molecule, and may be used in the design of complex nanostructures. The resonance peak of a metal nanoring is produced by the bonding mode at a greater wavelength and the anti-bonding mode at a shorter wavelength. These modes' resonance frequencies are highly dependent on the shell thickness. Due to poor interaction with incoming light and vibration dampening associated with interband transitions in the metal, the non-bonding mode does not show up in the observed spectra. When the center of the nanoring is relocated, a lower asymmetry permits the mixing of modes, resulting in a spectrum with several peaks [80]. When the core offset rises, peak widening and new peaks are anticipated to arise owing to the interaction between plasmonic resonance with various mode numbers (i.e., angular momentum).

Figure 4 presents the shift of the resonance peak for nanorings with different diameters, inner ring radius, and core offset for the refractive index of medium 1.4, which is near the refractive index of the common sensing medium. The supporting information shows that the trends for other refractive indexes between 1.0–2.0 are similar. The redshift of the resonances is visible when the nanoring diameter and inner ring radius increase. The increase in core offset also causes redshift, but not as high as those resulting from the diameter and inner ring radius increases. The redshift with core offset shows a nearly quadratic dependence on the normalized inner ring radius. A nearly quadratic redshift can be explained in the framework of the hybridization model. The dipolar resonance frequency of a shell structure is equal to the difference between cavity and disk plasmon modes. The interaction of hybridized modes is stronger for thinner shells

(or larger inner radius). Reduced shell thickness decreases the symmetric bonding mode frequency or is equivalent to the redshift of the resonance wavelength. Many previous studies reported a similar dependency of resonance wavelength on shell thickness. An analytical formula for the dependence of resonance frequency on shell thickness can be found in published works [68, 79, 81].

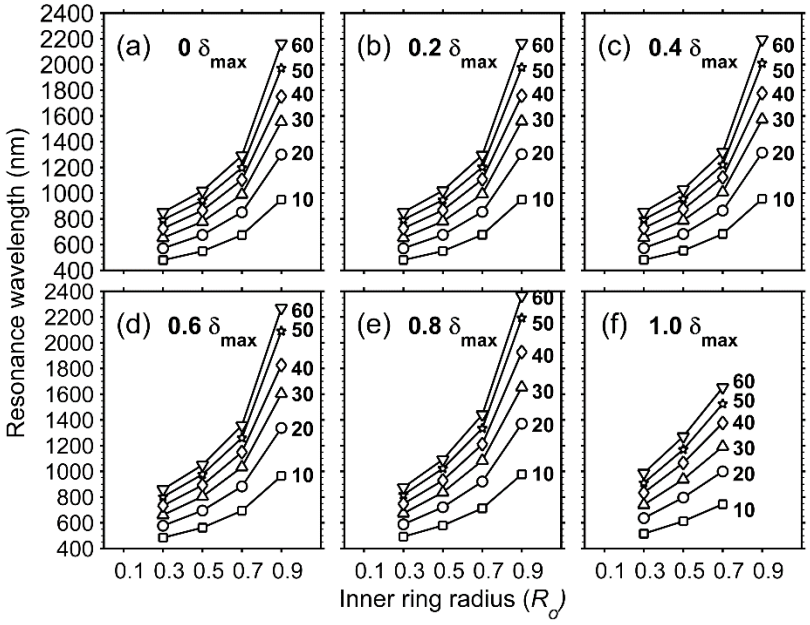

Figure 4. Resonance wavelength of the lowest order (dipolar) peak of nanoring as a function of inner ring radius for different nanoring core offset, (a) 0, (b) 0.2 δ_{max}, (c) 0.4 δ_{max}, (d) 0.6 δ_{max}, (e) 0.8 δ_{max}, and (f) δ_{max}. The refractive index was set to 1.4. Diameters of nanoring, in nanometers, are given in each plot.

Figure 5 depicts the resonance wavelength of different nanoring sizes as a function of core offset and medium refractive index. The diameter of the nanoring is shown above each column's graphs. In each row, the variation in shell thickness (inner ring radius) is displayed on the right side of the graph. A almost monotone colour gradient denotes a constant rise in the resonance wavelength as a function of nanoring diameter, inner ring diameter, core offset, and refractive index of the medium. The resonance wavelength may be modulated from the visible spectrum to the near-infrared spectrum, where biological applications are of significant interest.

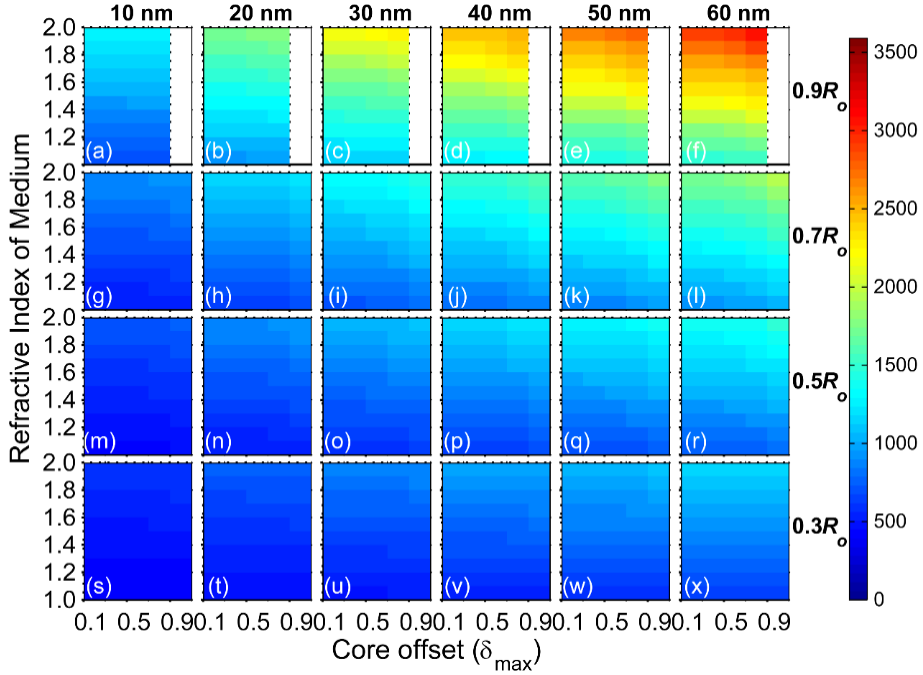

Figure 5. Resonance wavelength (in nanometer) map of the lowest order (dipolar) peak of nanoring as a function of core offset and refractive index of medium for nanoring with different diameter, (a, g, m, s) 10 nm, (b, h, n, t) 20 nm, (c, i, o, u) 30 nm, (d, j, p, v) 40 nm, (e, k, q, w) 50 nm, and (f, l, r, x) 60 nm. The scale bar color code is the same for all plots.

There are several reasons for the red shift of the resonance peak with increasing nanoring diameter, including 1) the retardation effect, 2) a size-dependent dielectric constant, and 3) a disturbance in electron density. When a particle's size exceeds 20 nm, the impact of retardation takes action. Depolarization of the electric field over the particle's surface causes retardation. Due to the varied route lengths traversed by the wave, the incident electromagnetic wave will be dispersed by nanoparticles with non-negligible phase discrepancies. The scattering of conduction electrons with the surface increases as the nanoparticle size decreases (i.e., the nanoparticle size is less than the effective electron path length). The complicated function of a metallic nanoparticle's dielectric constant may be described using the Drude model [82, 83], which considers the influence of this scattering. The position and strength of the resonance peak are mostly governed by the real component of the dielectric constant. The redshift may also be interpreted as a result of perturbations in the conduction electrons' density [84]. A nanoparticle of metal can be seen as a resonance box. A tiny nanoparticle indicates a small region for light to bounce. Hence, only a short wavelength can satisfy the quantization of angular momentum on the nanoparticle's surface. The opposite occurs with larger particles.

Surface plasmonic resonance is caused by two opposing forces: a driving force from an incoming electromagnetic wave and a restorative force between conduction electrons and positive ions of metal. The amplitude of the restoring force depends on the optical characteristics, size, and shape of the metal nanoparticle. The resonance moves to a longer wavelength when the refractive index of the medium around metal nanoparticles increases (decreasing resonance frequency). The shift is associated with the decrease in the restoring Coulombic force brought about by the increased shielding between the oscillating electrons and positive ions [42]. The shielding is caused by an increase in medium polarization, which diminishes the accumulated charge on the metal's surface. The decrease in restoring force reduces the electromagnetic wave energy necessary to induce coherent electron oscillation. Alternately, the dielectric constants of the metal and the surrounding medium provide the boundary conditions that must be satisfied to account for the redshift as the medium's refractive index rises. The boundary constraints stipulate that the electric field and electric potential must be continuous within and outside the nanoparticle. The dielectric function of metal nanoparticles is dependent on wavelength, whereas it is real and nondispersive in dielectric media. Therefore, as the surrounding dielectric constant (or refractive index) changes, the resonance condition adjusts.

The redshift as a function of the nanoring's shell thickness may be explained by plasmon hybridization between modes on the inner and outer shell surfaces. With a thinner shell, hybridization or interaction between modes is stronger. In this study, thinner corresponds to a bigger inner ring radius, as the outer ring radius was held constant throughout all variations. The hybridization splits the resonance into symmetric modes with lower energy and antisymmetric modes with greater energy for each angular momentum mode [56, 68]. Only the lowest symmetric mode substantially interacts with incoming light, resulting in a more prominent peak. Since the antisymmetric mode interacts with input light relatively slightly, it is not seen in the extinction spectra. As a result, a decrease in shell thickness causes the redshift of the symmetric mode.

In addition to resonance wavelength, redshift is followed by a broadening extinction peak. The width of the resonance peak is often measured by its full width at half of the maximum (or FWHM). The FWHM of nanoring with different diameters, inner ring radius, and core offset is given in Figure 6.

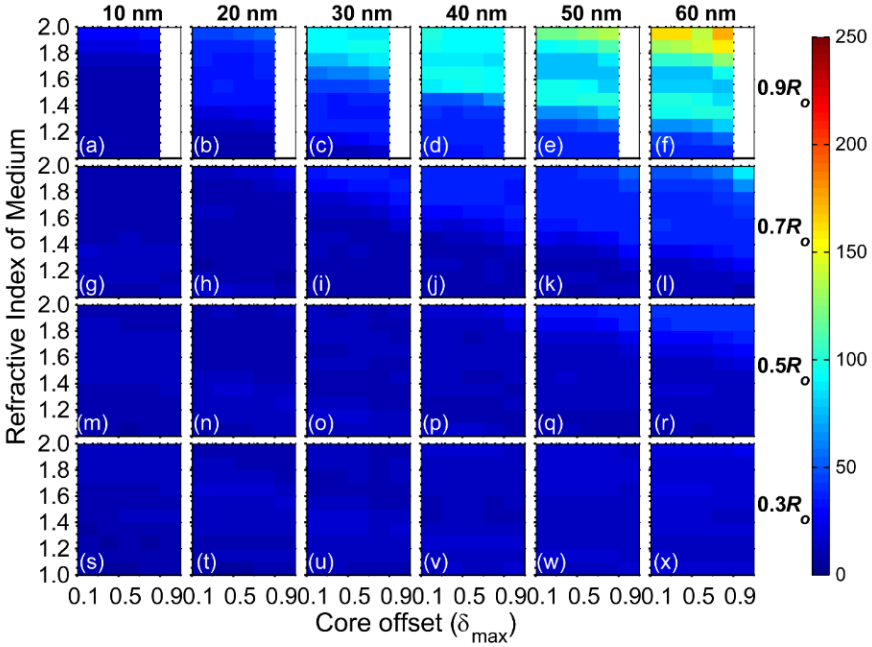

Figure 6. FWHM map of nanoring for different nanoring diameters as a function of core offset and refractive index of medium for nanoring with different diameter, (a, g, m, s) 10 nm, (b, h, n, t) 20 nm, (c, i, o, u) 30 nm, (d, j, p, v) 40 nm, (e, k, q, w) 50 nm, and (f, l, r, x) 60 nm. The scale bar color code is the same for all plots.

Gradation of the colormap indicates that larger nanoring diameter results in a broader peak. A broader extinction peak is also found for a thinner shell thickness (larger inner ring radius) and larger core offset. FWHM is less than 100 nm and suddenly increases when the inner ring radius is 0.9 R_o. Significant broadening is observed for nanoring with a diameter of 30–60 nm.

FWHM of shell structures like nanorings depends on 1) surface electron-surface scattering, 2) ratio of shell-to-core volume, 3) retardation, as well as 4) higher order modes contribution [85–87]. Electron–surface scattering is dominant for small nanoparticles whose diameter is smaller than the electron means free path. Nanoring with an outer diameter of 10 nm does not show significant broadening of the inner ring radius and core-offset variation (see Figure 6). Hence, surface scattering seems to be the most dominant factor for small nanorings. In contrast, peak broadening for a bigger nanoring is likely caused by radiation damping and retardation effects [82, 88]. Light does not arrive simultaneously to all electrons distributed in the volume of the nanoring. Consequently, scattered light from a different part of the nanoring has a non-negligible phase difference. The Interference of scattered light having phase differences causes rapid loss in coherent electron oscillation, resulting in peak broadening [84].

3-2- Sensing Sensitivity

The resonance wavelength shift depends quadratically on the medium's refractive index. Therefore, a linear relationship between sensitivity and refractive index is anticipated. This trend is generally acceptable, but has a different slope. The slope is determined by the nanoring's diameter, inner ring radius, and offset core. Figure 7 depicts the refractive index sensitivity of nanorings with varying diameters, inner ring radiuses, and core offsets. For each nanoring diameter, inner ring radius, and core offset, the sensitivity grows linearly with the refractive index. The increased sensing sensitivity of metal nanoparticles with a refractive index correlates with significant light amplification at the metal surface. The increased contribution of higher-order plasmonic modes may account for the rise in sensitivity with increasing dimension [87]. There have been reports of a linear increase in sensitivity with increasing nanoparticle diameter [42, 43, 87]. As the inner ring radius decreases, plasmonic mode interactions between the inner and outer surfaces of the nanoring shell increase, resulting in an increase in sensitivity. The rise of the real component of the dielectric function of core-shell nanoparticles [87] is another reason for the increased sensitivity with decreasing shell thickness. The enhanced sensitivity with decreasing shell thickness is consistent with the published literature [89, 90]. For inner ring radii of 0.7 R_o and 0.9 R_o, a considerable improvement in sensitivity is seen. The correlation between sensitivity and nanoparticle size is a larger scattering cross-section. A greater sensitivity in the infrared spectrum is well-known and consistent with several published investigations.

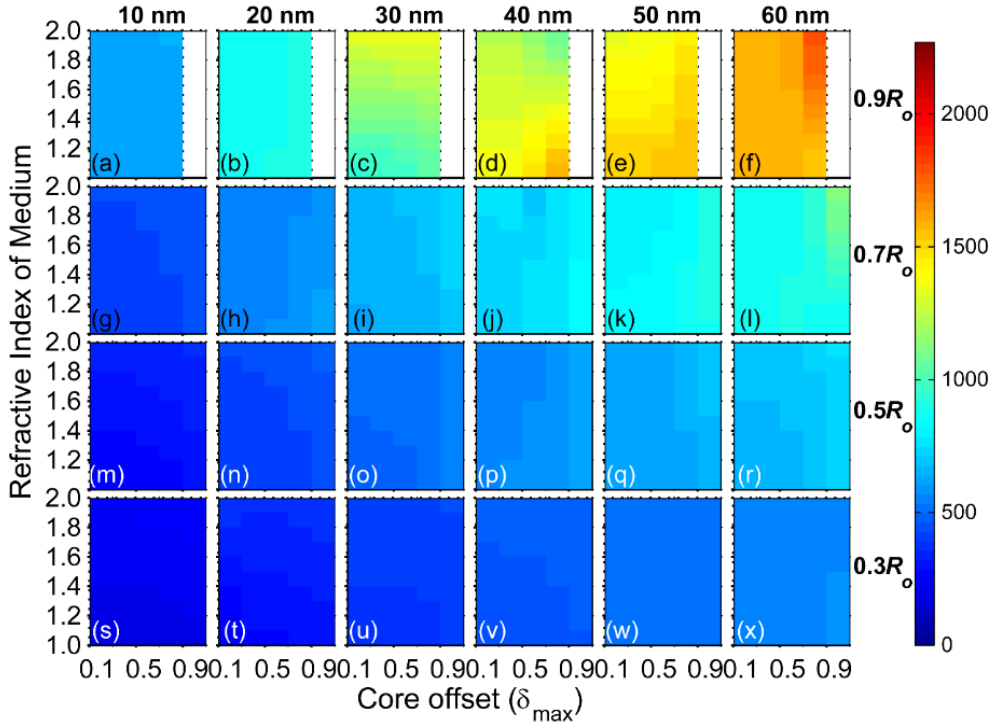

Figure 7. Sensitivity map of nanoring for different nanoring diameters as a function of core offset and refractive index of medium for nanoring with different diameter, (a, g, m, s) 10 nm, (b, h, n, t) 20 nm, (c, i, o, u) 30 nm, (d, j, p, v) 40 nm, (e, k, q, w) 50 nm, and (f, l, r, x) 60 nm. The scale bar color code is the same for all plots.

The obtained sensitivity in the simulation range is 170 – 2273 nm/RIU, which is much higher than the values reported in the literature for LSPR-based sensing. The obtained sensitivity is comparable to the standard propagating surface plasmon sensor. Some sensitivity values of nanoparticles reported in the literature are 100 – 600 nm/RIU for various core-shell structures (sphere, disk, rod, ellipsoid, prism) [87, 91], 385 nm/RIU for core-shell gold [92], 208 nm/RIU for solid disk [77], 50 – 172 nm/RIU for gold sphere [82, 92, 93], 801.4 nm/RIU and 103.0 nm/RIU for the longitudinal as well as transverse plasmon modes of core-shell rice [89], 150 – 352 nm/RIU for nanorod [94, 95], 405 – 425 nm/RIU for prism [96], 91 – 266 nm/RIU for cube [96], 315 nm/RIU for silver nanoplate [96]. The obtained value is even higher than observed for a periodic array of nanoparticles, namely 327 nm/RIU for disk [97], 1753 nm/RIU for crossed-bowtie nanostructure [32], and 685 nm/RIU for gold nanocylinders [98]. More data on the sensitivity of nanoparticles with various geometry can be found in a published review article [99, 100].

For the medium's fixed refractive index, the sensitivity increases almost linearly with nanoring diameter (see Figure 8). This trend is observed for all inner ring radii and core offsets. Despite a similar trend, the slope of the sensitivity on nanoring diameter is much steeper for thinner shells (i.e., larger inner ring radius). Sensitivity slightly increases with core offset for a fixed nanoring diameter and shell thickness. A higher sensitivity increase is evident for maximum core offset ($\delta=\delta_{max}$). The increase of sensitivity with core offset corresponds to the stronger interaction between the plasmonic modes of the core and the shell. Using different modes leads to a greater redshift of the bonding modes manifested in increased sensitivity. A thinner shell and larger core offset are advantageous for sensing applications.

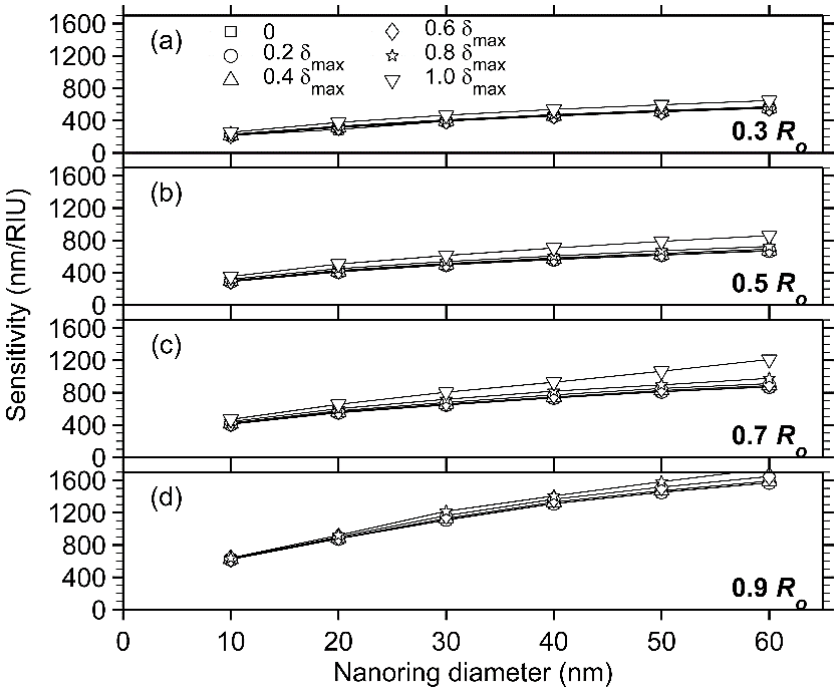

Figure 8. Sensitivity of nanoring as a function of nanoring diameter for different inner ring radii, (a) 0.3 R_o, (b) 0.5 R_o, (c) 0.7 R_o, and (d) 0.9 R_o. The legend for core offset is given in figure (a). The refractive index was set to 1.4. Symbols used as data markers are given in figure (a).

3-3- The Figure of Merit (FOM)

As discussed in the previous sections, the increase of sensitivity for a larger nanoring diameter, thinner shell, and large core offset is followed by the broadening of the resonance peak. Consequently, the sensing performance of an LSPR-based sensor could be further improved. Therefore, finding optimum geometry and size is essential. FOM of nanoring as refractive index sensor as a function of nanoring diameter, inner ring radius, and core offset is presented in Figure 9.

FOM tends to decrease with refractive index due to resonance peak broadening. The maximum FOM for each diameter tends to shift to a lower refractive index, smaller inner ring radius, and larger core offset. The maximum FOM for nanoring with a diameter of 10 nm has a single band peak in the FOM map. From the FOM map, we can see that the number of FOM peak band increase to four for diameter 20 – 60 nm that become more separated with the increase of nanoring diameter. The highest FOM of 170 RIU^{-1} is obtained for nanoring with a diameter of 20 nm and inner ring radius of 0.9 Ro when the surrounding medium is air (refractive index of 1.0). Usually, sensing is carried out at a solution with a refractive index between 1.5 – 1.5. In this range, high FOM is obtained for nanoring with a diameter around 30 – 40 nm with an inner radius of 0.7 R_o. Very high FOM for nanoring is related to a very sharp resonance peak (i.e., small FWHM).

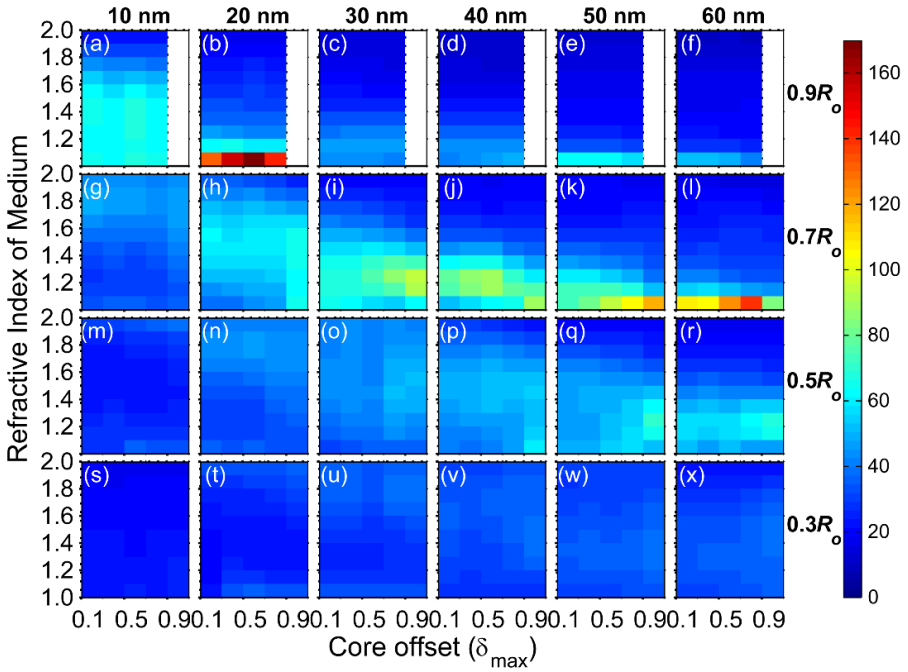

Figure 9. The figure of merit map of nanoring for different nanoring diameters as a function of core offset and refractive index of medium for nanoring with different diameter, (a, g, m, s) 10 nm, (b, h, n, t) 20 nm, (c, i, o, u) 30 nm, (d, j, p, v) 40 nm, (e, k, q, w) 50 nm, and (f, l, r, x) 60 nm. The scale bar color code is the same for all plots.

The obtained FOM for nanoring is much higher than that reported in most literature. The FOM of nanoparticles is 1.2 – 3 RIU^{-1} for sphere [96], 5.4 RIU^{-1} for cube-on-glass system [44], 3 – 3.8 RIU^{-1} for prism [96], 8.3 RIU^{-1} for gold disk [77], 2 – 2.6 RIU^{-1} for cube [96], and 3.6 RIU^{-1} for nanorod [96]. FOM of an array of nanoparticles is 9.87 RIU^{-1} for nanocylinder [98], 4 RIU^{-1} for disk heptamer [58], 3.65 RIU^{-1} for gold crossed-bowtie nanostructures [32], and 13.25 RIU^{-1} for Cu octamer [101]. More data for FOM of nanoparticles with various geometry can be found in a published review article [99, 100]. Higher FOM of nanoring biosensors corresponds to higher sensitivity and relatively narrow resonance peaks due to the excitation of Fano resonance for non-concentric nanoring. Fano resonance is excited in asymmetric or non-concentric nanoshell structures like nanoring [56, 68, 102].

The FOM values at a fixed medium refractive index for different nanoring diameters, inner ring radius, and core offset are plotted in Figure 10.

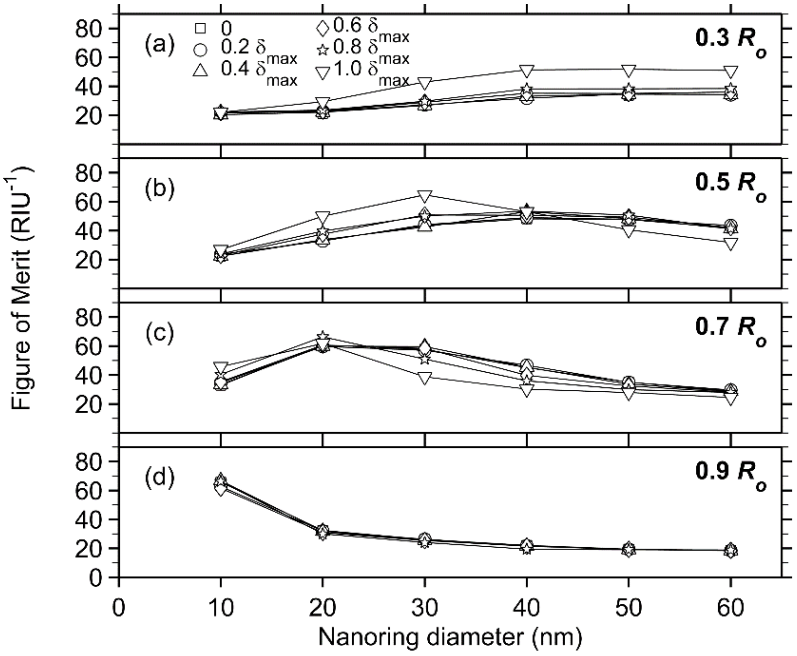

Figure 10. FOM of nanoring as a function of nanoring diameter for different inner ring radii, (a) 0.3 R_o, (b) 0.5 R_o, (c) 0.7 R_o, and (d) 0.9 R_o. The legend for core offset is given in figure (a). The refractive index was set to 1.4. Symbols used as data markers are given in figure (a).

This refractive index is in the range of biomolecular solutions. Strikingly different trends are apparent. The trend depends significantly on shell thickness. For a thick shell (R_i = 0.3 R_o), FOM increases linearly with nanoring diameter. For intermediate shell thickness (R_i = 0.5 R_o and R_i = 0.7 R_o), FOM increases for small nanoring and then decreases. The maximum FOM is obtained for a nanoring diameter of 20-30 nm. An exponential decrease of FOM is observed for a very thin shell (R_i = 0.9 R_o). The effect of core offset is minor for the thin shell because the nominal shift of the core is much smaller. FOM is affected more by FWHM than sensitivity. This result shows that maximum FOM depends on nanoring diameter and shell thickness in a complex manner.

3-4- General Scaling Law for Sensing Performance Parameters

In previous sections, large variations of sensing performances on nanoring diameter, inner ring radius, core offset, and medium's refractive index were discussed. Therefore, it is interesting to see general trends or scaling laws of the sensing performance parameters. First, we overlap all data for different geometrical and medium parameters in a single plot for each sensing parameter. Figures 11-a to 11-c shows how sensitivity, FWHM, and FOM change with material and medium properties represented by resonance wavelength. Despite the scattering of the data, the overall trends are apparent.

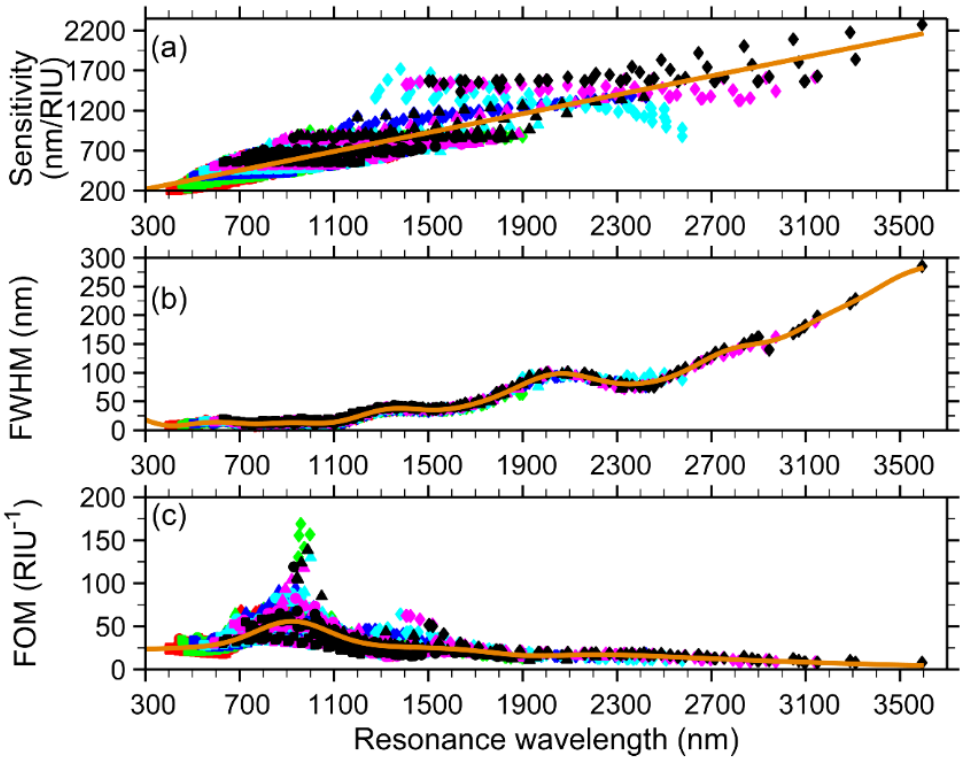

Figure 11. Dependence of sensing performance parameters on resonance wavelength, (a) sensitivity, (b) FWHM, and (c) FOM. All data for nanoring with different diameters are differentiated by color, 10 nm (in red), 20 nm (in green), 30 nm (in blue), 40 nm (in cyan), 50 nm (in magenta), and 60 nm (in black). All data for different inner ring radii are differentiated by data markers, 0.3 R_o (square), 0.5 R_o (circle), 0.7 R_o (triangle), and 0.9 R_o (diamond).

Sensitivity increases almost linearly with the resonance wavelength (i.e., nanoring diameter, inner ring diameter, and core offset) for all data sets. The nanoring with a thinner shell (R_i = 0.9 R_o) consistently shows higher sensitivity independent of nanoring diameter. A nonlinear increase of FWHM with resonance wavelength is evident. All FWHM data fit nicely with multiple sine addition functions. FOM data are the best fit with multiple gaussian addition functions. A broader resonance peak with particle size and reduced shell thickness is known and has been reported by many researchers. FOM has a maximum value of 180 RIU^{-1} for an intermediate resonance wavelength, vis – NIR. The FOM of nanoring is above 100 RIU^{-1} for a resonance wavelength of 900 – 1000 nm. FOM decreases at longer resonance wavelengths due to significant peak broadening. High sensitivity and FOM in the visible and NIR range that is desirable for any biological application, since human tissue in this region has the greatest degree of transparency.

The correlations between FWHM versus sensitivity and FOM are shown in Figure 12. Sensitivity and FWHM have a positive correlation, with the best fit satisfying function of $S = 7.6 \exp(0.00158 \cdot FWHM)$. On the contrary, FOM generally decreases with FWHM, with the best-fit function being power fit that is $FOM = 126 \cdot (FWHM)^{-0.4809} + 1.168$. This graph shows that FOM is affected stronger by FWHM than sensitivity. This figure also shows that large nanoring with a thin shell does not result in better sensing performance.

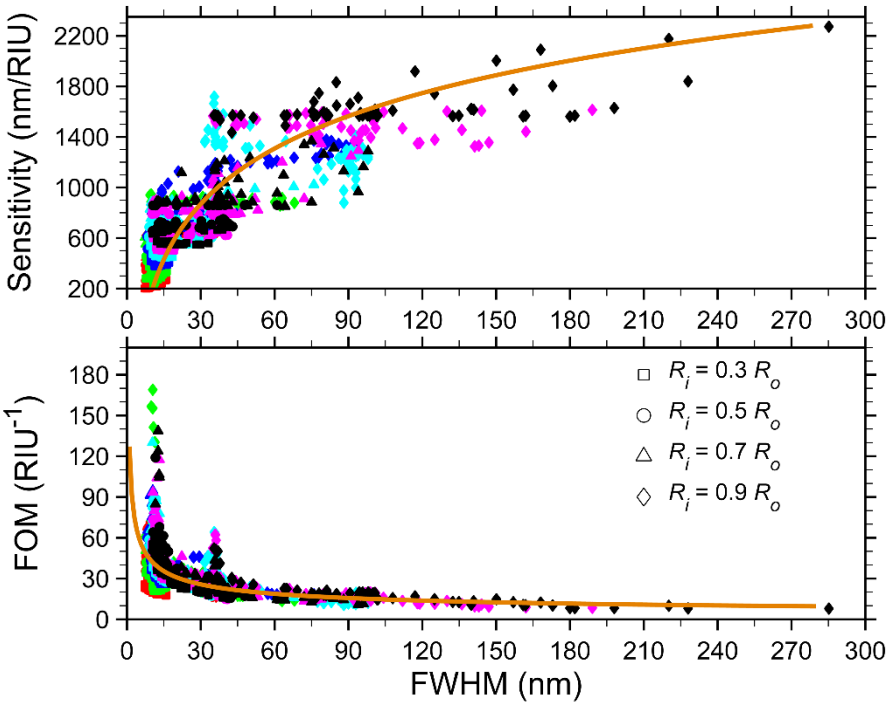

Figure 12. The correlation between FWHM and (a) sensitivity and (b) FOM. All data for nanoring with different diameters are differentiated by color, 10 nm (red), 20 nm (green), 30 nm (blue), 40 nm (cyan), 50 nm (magenta), and 60 nm (black). All data for different inner ring radii are differentiated by data markers, 0.3 R_o (square), 0.5 R_o (circle), 0.7 R_o (triangle), and 0.9 R_o (diamond).

4- Conclusion

Resonance wavelength, sensitivity, FWHM, and FOM depend significantly on the nanoring radius, inner ring diameter, core offset, and the medium's refractive index. Redshift and broadening of the resonance peak are observed with an increase in nanoring diameter, inner ring radius, and core offset. The red shift and broadening with nanoring diameter and refractive index of the medium arise from decreasing restoring force, retardation, depolarization, and damping. The effects of inner ring radius (i.e., the thickness of the nanoring shell) and core offset have been explained based on the hybridization model of plasmonic modes. Finally, it presents some correlations or scaling laws connecting sensing performance parameters for nanorings. Also, it is shown that nanorings have promising potential for sensing applications, as they offer great figures of merit and sensitivity as compared to nanoparticles with other geometries. The highest obtained sensitivity and FOM are 2272 nm/RIU and 170 RIU^{-1}, respectively. The values are much higher than most of the reported data in the literature for LSPR-based sensors. The high sensitivity and FOM of nanoring over the visible and NIR ranges make it highly suitable for biosensing applications.

5- Declarations

5-1- Author Contributions

Conceptualization, M.M.; methodology, M.M.; software, I.P.; formal analysis, E.E. and D.P.; data curation, I.P.; writing—original draft preparation, M.M.; writing—review and editing, M.M., E.E., and D.P.; funding acquisition, M.M. All authors have read and agreed to the published version of the manuscript.

5-2- Data Availability Statement

The data presented in this study are available on request from the corresponding author.

5-3- Funding

Research Contract No. T/11/UN.16.17/PP.IS-PDU-KRP2GB-Unand/2022.

5-4- Acknowledgements

Thanks to Universitas Andalas for the financial funding of this research.

5-5- Institutional Review Board Statement

Not applicable.

5-6- Informed Consent Statement

Not applicable.

5-7- Conflicts of Interest

The authors declare that there is no conflict of interest regarding the publication of this manuscript. In addition, the ethical issues, including plagiarism, informed consent, misconduct, data fabrication and/or falsification, double publication and/or submission, and redundancies have been completely observed by the authors.

6- References

[1] Li, X., Li, W., Guo, X., Lou, J., & Tong, L. (2013). All-fiber hybrid photon-plasmon circuits: integrating nanowire plasmonics with fiber optics. Optics Express, 21(13), 15698. doi:10.1364/oe.21.015698.

[2] Ricciardi, A., Crescitelli, A., Vaiano, P., Quero, G., Consales, M., Pisco, M., Esposito, E., & Cusano, A. (2015). Lab-on-fiber technology: A new vision for chemical and biological sensing. Analyst, 140(24), 8068–8079. doi:10.1039/c5an01241d.

[3] Wu, X., Zhou, L., Su, Y., & Dong, C. M. (2016). Plasmonic, Targeted, and Dual Drugs-Loaded Polypeptide Composite Nanoparticles for Synergistic Cocktail Chemotherapy with Photothermal Therapy. Biomacromolecules, 17(7), 2489–2501. doi:10.1021/acs.biomac.6b00721.

[4] Lazic, V., Palucci, A., De Dominicis, L., Nuvoli, M., Pistilli, M., Menicucci, I., Colao, F., & Almaviva, S. (2019). Integrated laser sensor (ILS) for remote surface analysis: Application for detecting explosives in fingerprints. Sensors (Switzerland), 19(19), 4269. doi:10.3390/s19194269.

[5] Shrivastav, A. M., Cvelbar, U., & Abdulhalim, I. (2021). A comprehensive review on plasmonic-based biosensors used in viral diagnostics. Communications Biology, 4(1), 1–12. doi:10.1038/s42003-020-01615-8.

[6] Kim, H. M., Park, J. H., & Lee, S. K. (2019). Fiber optic sensor based on ZnO nanowires decorated by Au nanoparticles for improved plasmonic biosensor. Scientific Reports, 9(1), 15605. doi:10.1038/s41598-019-52056-1.

[7] Javaid, M., Haleem, A., Singh, R. P., Rab, S., & Suman, R. (2021). Significance of sensors for industry 4.0: Roles, capabilities, and applications. Sensors International, 2, 100110. doi:10.1016/j.sintl.2021.100110.

[8] Bhattacharya, S., Agarwal, A. K., Prakash, O., & Singh, S. (2019). Sensors for Automotive and Aerospace Applications. Energy, Environment, and Sustainability, Springer, Singapore. doi:10.1007/978-981-13-3290-6.

[9] Rifat, A. A., Ahmed, R., Mahdiraji, G. A., & Adikan, F. R. M. (2017). Highly sensitive D-shaped photonic crystal fiber-based plasmonic biosensor in visible to near-IR. IEEE Sensors Journal, 17(9), 2776–2783. doi:10.1109/JSEN.2017.2677473.

[10] Fan, M., Andrade, G. F. S., & Brolo, A. G. (2020). A review on recent advances in the applications of surface-enhanced Raman scattering in analytical chemistry. Analytica Chimica Acta, 1097, 1–29. doi:10.1016/j.aca.2019.11.049.

[11] Bülbül, G., Hayat, A., & Andreescu, S. (2015). Portable nanoparticle-based sensors for food safety assessment. Sensors (Switzerland), 15(12), 30736–30758. doi:10.3390/s151229826.

[12] Mehrotra, P. (2016). Biosensors and their applications - A review. Journal of Oral Biology and Craniofacial Research, 6(2), 153–159. doi:10.1016/j.jobcr.2015.12.002.

[13] Zheng, Y., Bian, S., Sun, J., Wen, L., Rong, G., & Sawan, M. (2022). Label-Free LSPR-Vertical Microcavity Biosensor for On-Site SARS-CoV-2 Detection. Biosensors, 12(3), 151. doi:10.3390/bios12030151.

[14] Justino, C. I. L., Duarte, A. C., & Rocha-Santos, T. A. P. (2017). Recent progress in biosensors for environmental monitoring: A review. Sensors (Switzerland), 17(12), 2918. doi:10.3390/s17122918.

[15] Liu, J., Jalali, M., Mahshid, S., & Wachsmann-Hogiu, S. (2020). Are plasmonic optical biosensors ready for use in point-of-need applications? Analyst, 145(2), 364–384. doi:10.1039/c9an02149c.

[16] Justino, C. I. L., Rocha-Santos, T. A., & Duarte, A. C. (2010). Review of analytical figures of merit of sensors and biosensors in clinical applications. TrAC - Trends in Analytical Chemistry, 29(10), 1172–1183. doi:10.1016/j.trac.2010.07.008.

[17] Anas, N. A. A., Fen, Y. W., Omar, N. A. S., Daniyal, W. M. E. M. M., Ramdzan, N. S. M., & Saleviter, S. (2019). Development of Graphene Quantum Dots-Based Optical Sensor for Toxic Metal Ion Detection. Sensors, 19(18), 3850. doi:10.3390/s19183850.

[18] Stewart, M. E., Anderton, C. R., Thompson, L. B., Maria, J., Gray, S. K., Rogers, J. A., & Nuzzo, R. G. (2008). Nanostructured plasmonic sensors. Chemical Reviews, 108(2), 494–521. doi:10.1021/cr068126n.

[19] Tong, L. M., & Xu, H. X. (2012). Surface plasmons-mechanisms, application and perspectives. Physics, 41(9), 582-588.

[20] Svedendahl, M., Chen, S., Dmitriev, A., & Käll, M. (2009). Refractometric sensing using propagating versus localized surface plasmons: A direct comparison. Nano Letters, 9(12), 4428–4433. doi:10.1021/nl902721z.

[21] Haes, A. J., & Van Duyne, R. P. (2002). A nanoscale optical biosensor: Sensitivity and selectivity of an approach based on the localized surface plasmon resonance spectroscopy of triangular silver nanoparticles. Journal of the American Chemical Society, 124(35), 10596–10604. doi:10.1021/ja020393x.

[22] Alivisatos, P. (2004). The use of nanocrystals in biological detection. Nature Biotechnology, 22(1), 47–52. doi:10.1038/nbt927.

[23] Aizpurua, J., Bryant, G. W., Richter, L. J., García de Abajo, F. J., Kelley, B. K., & Mallouk, T. (2005). Optical properties of coupled metallic nanorods for field-enhanced spectroscopy. Physical Review B, 71(23). doi:10.1103/physrevb.71.235420.

[24] Le, F., Brandl, D. W., Urzhumov, Y. A., Wang, H., Kundu, J., Halas, N. J., Aizpurua, J., & Nordlander, P. (2008). Metallic nanoparticle arrays: A common substrate for both surface-enhanced Raman scattering and surface-enhanced infrared absorption. ACS Nano, 2(4), 707–718. doi:10.1021/nn800047e.

[25] Nakayama, K., Tanabe, K., & Atwater, H. A. (2008). Plasmonic nanoparticle enhanced light absorption in GaAs solar cells. Applied Physics Letters, 93(12), 121904. doi:10.1063/1.2988288.

[26] Perdana, I., & Muldarisnur, M. (2021). Optimization of Ag-SiO2 core-shell nanoparticles arrangement for light absorption enhancement in organic solar cells. AIP Conference Proceedings. doi10.1063/5.0037507.

[27] Aćimović, S. S., Ortega, M. A., Sanz, V., Berthelot, J., Garcia-Cordero, J. L., Renger, J., Maerkl, S. J., Kreuzer, M. P., & Quidant, R. (2014). LSPR chip for parallel, rapid, and sensitive detection of cancer markers in serum. Nano Letters, 14(5), 2636–2641. doi:10.1021/nl500574n.

[28] Turcheniuk, K., Dumych, T., Bilyy, R., Turcheniuk, V., Bouckaert, J., Vovk, V., Chopyak, V., Zaitsev, V., Mariot, P., Prevarskaya, N., Boukherroub, R., & Szunerits, S. (2016). Plasmonic photothermal cancer therapy with gold nanorods/reduced graphene oxide core/shell nanocomposites. RSC Advances, 6(2), 1600–1610. doi:10.1039/c5ra24662h.

[29] Yildiz, A. A. (2016). On-Chip Drug Screening and Nanomedicine Applications via (L)SPR. Journal of Nanomedicine Research, 4(4), 94. doi:10.15406/jnmr.2016.04.00094.

[30] Suarez, M. A., Grosjean, T., Charraut, D., & Courjon, D. (2007). Nanoring as a magnetic or electric field sensitive nano-antenna for near-field optics applications. Optics Communications, 270(2), 447–454. doi:10.1016/j.optcom.2006.09.020.

[31] Hong, Y., Huh, Y. M., Yoon, D. S., & Yang, J. (2012). Nanobiosensors based on localized surface plasmon resonance for biomarker detection. Journal of Nanomaterials, 2012. doi:10.1155/2012/759830.

[32] Das, A., Kumar, K., & Dhawan, A. (2021). Periodic arrays of plasmonic crossed-bowtie nanostructures interspaced with plasmonic nanocrosses for highly sensitive LSPR based chemical and biological sensing. RSC Advances, 11(14), 8096–8106. doi:10.1039/d0ra09012c.

[33] Zalyubovskiy, S. J., Bogdanova, M., Deinega, A., Lozovik, Y., Pris, A. D., An, K. H., Hall, W. P., & Potyrailo, R. A. (2012). Theoretical limit of localized surface plasmon resonance sensitivity to local refractive index change and its comparison to conventional surface plasmon resonance sensor. Journal of the Optical Society of America A, 29(6), 994. doi:10.1364/josaa.29.000994.

[34] Homola, J. (2008). Surface plasmon resonance sensors for detection of chemical and biological species. Chemical Reviews, 108(2), 462–493. doi:10.1021/cr068107d.

[35] Liang, Y., Zhang, H., Zhu, W., Agrawal, A., Lezec, H., Li, L., Peng, W., Zou, Y., Lu, Y., & Xu, T. (2017). Subradiant Dipolar Interactions in Plasmonic Nanoring Resonator Array for Integrated Label-Free Biosensing. ACS Sensors, 2(12), 1796–1804. doi:10.1021/acssensors.7b00607.

[36] Nguyen, H. H., Park, J., Kang, S., & Kim, M. (2015). Surface plasmon resonance: A versatile technique for biosensor applications. Sensors (Switzerland), 15(5), 10481–10510. doi:10.3390/s150510481.

[37] Willets, K. A., & Van Duyne, R. P. (2007). Localized surface plasmon resonance spectroscopy and sensing. Annual Review of Physical Chemistry, 58, 267–297. doi:10.1146/annurev.physchem.58.032806.104607.

[38] Anker, J. N., Hall, W. P., Lyandres, O., Shah, N. C., Zhao, J., & Van Duyne, R. P. (2008). Biosensing with plasmonic nanosensors. Nature Materials, 7(6), 442–453. doi:10.1038/nmat2162.

[39] Kazuma, E., & Tatsuma, T. (2014). Localized surface plasmon resonance sensors based on wavelength-tunable spectral dips. Nanoscale, 6(4), 2397–2405. doi:10.1039/c3nr05846h.

[40] Hamza, M. E., Othman, M. A., & Swillam, M. A. (2022). Plasmonic Biosensors: Review. Biology, 11(5), 621. doi:10.3390/biology11050621.

[41] Wiley, B. J., Im, S. H., Li, Z. Y., McLellan, J., Siekkinen, A., & Xia, Y. (2006). Maneuvering the surface plasmon resonance of silver nanostructures through shape-controlled synthesis. Journal of Physical Chemistry B, 110(32), 15666–15675. doi:10.1021/jp0608628.

[42] Muldarisnur, M., Oktorina, E., Fridayanti, N., Zeni, E., Elvaswer, E., & Syukri, S. (2019). Size and aspect ratio dependency of sensitivity of ellipsoidal metal nanoparticle based liquid sensor. IOP Conference Series: Materials Science and Engineering, 578(1), 12035. doi:10.1088/1757-899X/578/1/012035.

[43] Muldarisnur, M., Fridayanti, N., Oktorina, E., Zeni, E., Elvaswer, E., & Syukri, S. (2019). Effect of nanoparticle geometry on sensitivity of metal nanoparticle based sensor. IOP Conference Series: Materials Science and Engineering, 578(1), 12036. doi:10.1088/1757-899X/578/1/012036.

[44] Sherry, L. J., Chang, S. H., Schatz, G. C., Van Duyne, R. P., Wiley, B. J., & Xia, Y. (2005). Localized surface plasmon resonance spectroscopy of single silver nanocubes. Nano Letters, 5(10), 2034–2038. doi:10.1021/nl0515753.

[45] Chen, H., Shao, L., Li, Q., & Wang, J. (2013). Gold nanorods and their plasmonic properties. Chemical Society Reviews, 42(7), 2679–2724. doi:10.1039/c2cs35367a.

[46] Jakab, A., Rosman, C., Khalavka, Y., Becker, J., Trügler, A., Hohenester, U., & Sönnichsen, C. (2011). Highly sensitive plasmonic silver nanorods. ACS Nano, 5(9), 6880–6885. doi:10.1021/nn200877b.

[47] Wiley, B. J., Chen, Y., McLellan, J. M., Xiong, Y., Li, Z. Y., Ginger, D., & Xia, Y. (2007). Synthesis and optical properties of silver nanobars and nanorice. Nano Letters, 7(4), 1032–1036. doi:10.1021/nl070214f.

[48] Washio, I., Xiong, Y., Yin, Y., & Xia, Y. (2006). Reduction by the end groups of poly(vinyl pyrrolidone): A new and versatile route to the kinetically controlled synthesis of Ag triangular nanoplates. Advanced Materials, 18(13), 1745–1749. doi:10.1002/adma.200600675.

[49] Pastoriza-Santos, I., & Liz-Marzán, L. M. (2002). Synthesis of Silver Nanoprisms in DMF. Nano Letters, 2(8), 903–905. doi:10.1021/nl025638i.

[50] Hao, E., Bailey, R. C., Schatz, G. C., Hupp, J. T., & Li, S. (2004). Synthesis and Optical Properties of "Branched" Gold Nanocrystals. Nano Letters, 4(2), 327–330. doi:10.1021/nl0351542.

[51] Zhang, Q., Large, N., & Wang, H. (2014). Gold nanoparticles with tipped surface structures as substrates for single-particle surface-enhanced raman spectroscopy: Concave nanocubes, nanotrisoctahedra, and nanostars. ACS Applied Materials and Interfaces, 6(19), 17255–17267. doi:10.1021/am505245z.

[52] Nehl, C. L., Liao, H., & Hafner, J. H. (2006). Optical properties of star-shaped gold nanoparticles. Nano Letters, 6(4), 683–688. doi:10.1021/nl052409y.

[53] Huang, C., Ye, J., Wang, S., Stakenborg, T., & Lagae, L. (2012). Gold nanoring as a sensitive plasmonic biosensor for on-chip DNA detection. Applied Physics Letters, 100(17), 173114. doi:10.1063/1.4707382.

[54] Mu, S., Chen, H., Shi, C., Zhang, J., & Yang, B. (2021). Au nanoring arrays with tunable morphological features and plasmonic resonances. Nano Research, 14(12), 4674–4679. doi:10.1007/s12274-021-3402-3.

[55] Sonnefraud, Y., Verellen, N., Sobhani, H., Vandenbosch, G. A. E., Moshchalkov, V. V., Van Dorpe, P., Nordlander, P., & Maier, S. A. (2010). Experimental realization of subradiant, superradiant, and fano resonances in ring/disk plasmonic nanocavities. ACS Nano, 4(3), 1664–1670. doi:10.1021/nn901580r.

[56] Hao, F., Sonnefraud, Y., Dorpe, P. V., Maier, S. A., Halas, N. J., & Nordlander, P. (2008). Symmetry Breaking in Plasmonic Nanocavities: Subradiant LSPR Sensing and a Tunable Fano Resonance. Nano Letters, 8(11), 3983–3988. doi:10.1021/nl802509r.

[57] Fan, J. A., Wu, C., Bao, K., Bao, J., Bardhan, R., Halas, N. J., Manoharan, V. N., Nordlander, P., Shvets, G., & Capasso, F. (2010). Self-assembled plasmonic nanoparticle clusters. Science, 328(5982), 1135–1138. doi:10.1126/science.1187949.

[58] Lassiter, J. B., Sobhani, H., Fan, J. A., Kundu, J., Capasso, F., Nordlander, P., & Halas, N. J. (2010). Fano resonances in plasmonic nanoclusters: Geometrical and chemical tunability. Nano Letters, 10(8), 3184–3189. doi:10.1021/nl102108u.

[59] Kamarauskas, A., Seliuta, D., Šlekas, G., Sadauskas, M., Kvietkauskas, E., Trusovas, R., Ratautas, K., & Kancleris, Ž. (2022). Experimental demonstration of multiple Fano resonances in a mirrored array of split-ring resonators on a thick substrate. Scientific Reports, 12(1), 15846. doi:10.1038/s41598-022-20434-x.

[60] Rahmani, M., Luk'yanchuk, B., & Hong, M. (2013). Fano resonance in novel plasmonic nanostructures. Laser and Photonics Reviews, 7(3), 329–349. doi:10.1002/lpor.201200021.

[61] Dana, B. D., Koya, A. N., Song, X., & Lin, J. (2022). Enhanced FANO resonance in asymmetric nano dimer for sensing applications. Physica B: Condensed Matter, 631, 413706. doi:10.1016/j.physb.2022.413706.

[62] Roshani, S., Coccia, M., & Mosleh, M. (2022). Sensor Technology for Opening New Pathways in Diagnosis and Therapeutics of Breast, Lung, Colorectal and Prostate Cancer. HighTech and Innovation Journal, 3(3), 356-375. doi:10.28991/HIJ-2022-03-03-010.

[63] Agharazy Dormeny, A., Abedini Sohi, P., & Kahrizi, M. (2020). Design and simulation of a refractive index sensor based on SPR and LSPR using gold nanostructures. Results in Physics, 16, 102869. doi:10.1016/j.rinp.2019.102869.

[64] Khoshdel, V., & Shokooh-Saremi, M. (2019). Plasmonic nano bow-tie arrays with enhanced LSPR refractive index sensing. Micro and Nano Letters, 14(5), 566–571. doi:10.1049/mnl.2018.5588.

[65] An, T., Wen, J., Dong, Z., Zhang, Y., Zhang, J., Qin, F., Wang, Y., & Zhao, X. (2023). Plasmonic Biosensors with Nanostructure for Healthcare Monitoring and Diseases Diagnosis. Sensors, 23(1), 445. doi:10.3390/s23010445.

[66] Quintanilla-Villanueva, G. E., Maldonado, J., Luna-Moreno, D., Rodríguez-Delgado, J. M., Villarreal-Chiu, J. F., & Rodríguez-Delgado, M. M. (2023). Progress in Plasmonic Sensors as Monitoring Tools for Aquaculture Quality Control. Biosensors, 13(1), 90. doi:10.3390/bios13010090.

[67] Hu, Y., Noelck, S. J., & Drezek, R. A. (2010). Symmetry breaking in gold-silica-gold multilayer nanoshells. ACS Nano, 4(3), 1521–1528. doi:10.1021/nn901743m.

[68] Wu, Y., & Nordlander, P. (2006). Plasmon hybridization in nanoshells with a nonconcentric core. Journal of Chemical Physics, 125(12), 124708. doi:10.1063/1.2352750.

[69] Mangini, F., Tedeschi, N., Frezza, F., & Sihvola, A. (2014). Electromagnetic interaction with two eccentric spheres. Journal of the Optical Society of America A, 31(4), 783. doi:10.1364/josaa.31.000783.

[70] Johnson, P. B., & Christy, R. W. (1972). Optical constants of the noble metals. Physical Review B, 6(12), 4370–4379. doi:10.1103/PhysRevB.6.4370.

[71] García de Abajo, F. J., & Howie, A. (2002). Retarded field calculation of electron energy loss in inhomogeneous dielectrics. Physical Review B, 65(11). doi:10.1103/physrevb.65.115418.

[72] Hohenester, U., & Trugler, A. (2008). Interaction of Single Molecules with Metallic Nanoparticles. IEEE Journal of Selected Topics in Quantum Electronics, 14(6), 1430–1440. doi:10.1109/jstqe.2008.2007918.

[73] Hohenester, U., & Trügler, A. (2012). MNPBEM - A Matlab toolbox for the simulation of plasmonic nanoparticles. Computer Physics Communications, 183(2), 370–381. doi:10.1016/j.cpc.2011.09.009.

[74] Hohenester, U. (2014). Simulating electron energy loss spectroscopy with the MNPBEM toolbox. Computer Physics Communications, 185(3), 1177–1187. doi:10.1016/j.cpc.2013.12.010.

[75] Bonyár, A. (2021). Maximizing the surface sensitivity of lspr biosensors through plasmon coupling—interparticle gap optimization for dimers using computational simulations. Biosensors, 11(12), 527. doi:10.3390/bios11120527.

[76] Liu, Z., Liu, G., Liu, X., & Fu, G. (2020). Plasmonic sensors with an ultra-high figure of merit. Nanotechnology, 31(11), 115208. doi:10.1088/1361-6528/ab5a00.

[77] Lodewijks, K., Van Roy, W., Borghs, G., Lagae, L., & Van Dorpe, P. (2012). Boosting the figure-of-merit of LSPR-based refractive index sensing by phase-sensitive measurements. Nano Letters, 12(3), 1655–1659. doi:10.1021/nl300044a.

[78] Juvé, V., Cardinal, M. F., Lombardi, A., Crut, A., Maioli, P., Pérez-Juste, J., Liz-Marzán, L. M., Del Fatti, N., & Vallée, F. (2013). Size-dependent surface plasmon resonance broadening in nonspherical nanoparticles: Single gold nanorods. Nano Letters, 13(5), 2234–2240. doi:10.1021/nl400777y.

[79] Prodan, E., & Nordlander, P. (2004). Plasmon hybridization in spherical nanoparticles. Journal of Chemical Physics, 120(11), 5444–5454. doi:10.1063/1.1647518.

[80] Wang, H., Wu, Y., Lassiter, B., Nehl, C. L., Hafner, J. H., Nordlander, P., & Halas, N. J. (2006). Symmetry breaking in individual plasmonic nanoparticles. Proceedings of the National Academy of Sciences, 103(29), 10856–10860. doi:10.1073/pnas.0604003103.

[81] Prodan, E., & Nordlander, P. (2003). Structural tunability of the plasmon resonances in metallic nanoshells. Nano Letters, 3(4), 543–547. doi:10.1021/nl034030m.

[82] Farooq, S., & de Araujo, R. E. (2018). Engineering a Localized Surface Plasmon Resonance Platform for Molecular Biosensing. Open Journal of Applied Sciences, 08(03), 126–139. doi:10.4236/ojapps.2018.83010.

[83] Hutter, E., & Fendler, J. H. (2004). Exploitation of localized surface plasmon resonance. Advanced Materials, 16(19), 1685–1706. doi:10.1002/adma.200400271.

[84] Link, S., & El-Sayed, M. A. (2000). Shape and size dependence of radiative, non-radiative and photothermal properties of gold nanocrystals. International Reviews in Physical Chemistry, 19(3), 409–453. doi:10.1080/01442350050034180.

[85] Lee, K. S., & El-Sayed, M. A. (2006). Gold and silver nanoparticles in sensing and imaging: Sensitivity of plasmon response to size, shape, and metal composition. Journal of Physical Chemistry B, 110(39), 19220–19225. doi:10.1021/jp062536y.

[86] Westcott, S. L., Jackson, J. B., Radloff, C., & Halas, N. J. (2002). Relative contributions to the plasmon line shape of metal nanoshells. Physical Review B, 66(15). doi:10.1103/physrevb.66.155431.

[87] Shabaninezhad, M., & Ramakrishna, G. (2019). Theoretical investigation of size, shape, and aspect ratio effect on the LSPR sensitivity of hollow-gold nanoshells. Journal of Chemical Physics, 150(14), 144116. doi:10.1063/1.5090885.

[88] Hu, M., Novo, C., Funston, A., Wang, H., Staleva, H., Zou, S., Mulvaney, P., Xia, Y., & Hartland, G. V. (2008). Dark-field microscopy studies of single metal nanoparticles: Understanding the factors that influence the linewidth of the localized surface plasmon resonance. Journal of Materials Chemistry, 18(17), 1949–1960. doi:10.1039/b714759g.

[89] Wang, H., Brandl, D. W., Le, F., Nordlander, P., & Halas, N. J. (2006). Nanorice: A hybrid plasmonic nanostructure. Nano Letters, 6(4), 827–832. doi:10.1021/nl060209w.

[90] Jain, P. K., & El-Sayed, M. A. (2007). Surface plasmon resonance sensitivity of metal nanostructures: Physical basis and universal scaling in metal nanoshells. Journal of Physical Chemistry C, 111(47), 17451–17454. doi:10.1021/jp0773177.

[91] Sun, Y., & Xia, Y. (2002). Increased sensitivity of surface plasmon resonance of gold nanoshells compared to that of gold solid colloids in response to environmental changes. Analytical Chemistry, 74(20), 5297–5305. doi:10.1021/ac0258352.

[92] Fernandes, J., & Kang, S. (2021). Numerical study on the surface plasmon resonance tunability of spherical and non-spherical core-shell dimer nanostructures. Nanomaterials, 11(7). doi:10.3390/nano11071728.

[93] Farooq, S., Wali, F., Zezell, D. M., de Araujo, R. E., & Rativa, D. (2022). Optimizing and Quantifying Gold Nanospheres Based on LSPR Label-Free Biosensor for Dengue Diagnosis. Polymers, 14(8). doi:10.3390/polym14081592.

[94] Chen, Y., & Ming, H. (2012). Review of surface plasmon resonance and localized surface plasmon resonance sensor? Photonic Sensors, 2(1), 37–49. doi:10.1007/s13320-011-0051-2.

[95] Ratnawati, R., Wulandari, R., Kumoro, A. C., & Hadiyanto, H. (2022). Response surface methodology for formulating PVA/starch/lignin biodegradable plastic. Emerging Science Journal, 6(2), 238-255. doi:10.28991/ESJ-2022-06-02-03.

[96] Martinsson, E., Shahjamali, M. M., Enander, K., Boey, F., Xue, C., Aili, D., & Liedberg, B. (2013). Local refractive index sensing based on edge gold-coated silver nanoprisms. Journal of Physical Chemistry C, 117(44), 23148–23154. doi:10.1021/jp408187e.

[97] Lee, S. W., Lee, K. S., Ahn, J., Lee, J. J., Kim, M. G., & Shin, Y. B. (2011). Highly sensitive biosensing using arrays of plasmonic Au nanodisks realized by nanoimprint lithography. ACS Nano, 5(2), 897–904. doi:10.1021/nn102041m.

[98] Thilsted, A. H., Pan, J. Y., Wu, K., Zór, K., Rindzevicius, T., Schmidt, M. S., & Boisen, A. (2016). Lithography-Free Fabrication of Silica Nanocylinders with Suspended Gold Nanorings for LSPR-Based Sensing. Small, 12(48), 6745–6752. doi:10.1002/smll.201602299.

[99] Xu, Y., Bai, P., Zhou, X., Akimov, Y., Png, C. E., Ang, L. K., Knoll, W., & Wu, L. (2019). Optical Refractive Index Sensors with Plasmonic and Photonic Structures: Promising and Inconvenient Truth. Advanced Optical Materials, 7(9), 1801433. doi:10.1002/adom.201801433.

[100] Minopoli, A., Acunzo, A., Della Ventura, B., & Velotta, R. (2022). Nanostructured Surfaces as Plasmonic Biosensors: A Review. Advanced Materials Interfaces, 9(2), 2101133. doi:10.1002/admi.202101133.

[101] Ahmadivand, A., & Pala, N. (2015). Plasmon resonance hybridization in self-assembled copper nanoparticle clusters: Efficient and precise localization of surface plasmon resonance (LSPR) sensing based on FANO resonances. Applied Spectroscopy, 69(2), 277–286. doi:10.1366/14-07589.

[102] Hao, F., Nordlander, P., Sonnefraud, Y., Van Dorpe, P., & Maier, S. A. (2009). Tunability of subradiant dipolar and fano-type plasmon resonances in metallic ring/disk cavities: Implications for nanoscale optical sensing. ACS Nano, 3(3), 643–652. doi:10.1021/nn900012r.